

Cracking Mechanisms in Thermally Cycled Ti-6Al-4V Reinforced with SiC Fibers

S.H. THOMIN, P.A. NOËL, and D.C. DUNAND

A titanium alloy (Ti-6Al-4V) reinforced with continuous SiC fibers (SCS-6) was thermally cycled between 200 °C and 700 °C in air and argon. The composite mechanical properties deteriorate with an increasing number of cycles in air because of matrix cracks emanating from the specimen surface. These cracks also give oxygen access to fibers, further resulting in fiber degradation. The following matrix cracking mechanisms are examined: (1) thermal fatigue by internal stresses resulting from the mismatch of thermal expansion between fibers and matrix, (2) matrix oxygen embrittlement, and (3) ratcheting from oxide accumulating within cracks. Matrix stresses are determined using an analytical model, considering stress relaxation by matrix creep and the temperature dependence of materials properties. Matrix fatigue from these cyclically varying stresses (mechanism (1)) cannot solely account for the observed crack depth; oxygen embrittlement of the crack tip (mechanism (2)) is concluded to be another necessary damage mechanism. Furthermore, an approximate solution for the stress intensity resulting from crack wedging by oxide formation (mechanism (3)) is given, which may be an operating mechanism as well for long cracks.

I. INTRODUCTION

TITANIUM-base metal matrix composites (MMCs) exhibit high specific mechanical properties at room and elevated temperatures. However, the mismatch of thermal expansion between matrix and reinforcement induces thermal stresses upon temperature cycling,^[1] as described in what follows for titanium alloys reinforced with SCS-6 silicon carbide fibers.

Ritter *et al.*^[2] investigated a SCS-6/Ti-24Al-11Nb intermetallic matrix composite after thermal cycling between 25 °C and 760 °C. Cycling in air resulted in significantly more rapid degradation of the composite than isothermal aging or cycling in argon, due to matrix surface embrittlement and fiber delamination, deterioration, or breakage. Studying the same composite system, Russ^[3] found that cracks perpendicular to the fiber axis were initiating at the specimen surface and growing inward, reaching the fibers with increasing number of cycles. Radial cracks, present in the fiber/matrix interfacial reaction zone in the as-received state, also grew into the matrix. By varying the temperature range of the thermal cycling while keeping the maximum temperature constant, Russ showed that a minimum temperature range (*i.e.*, stress range) was necessary to induce cracking. Oxidation was a necessary condition as well, since no transverse cracking was observed when the maximum temperature was kept below that at which oxidation rates became significant. This was confirmed by Revelos and

Smith,^[4] who observed neither cracking nor property degradation after argon cycling of the same composite system. Extensive air cycling of SCS-6/Ti-15V-3Al-3Sn-3Cr MMC at temperatures where oxidation is low led to cracking at flaws in the matrix, on the edges of the sample, within the reaction zone of closely spaced fibers, and in the fiber row closest to the free surface.^[5-7] In composites with Ti-6Al-4V matrices, air cycling between room temperature and 550 °C induced thicker interface reaction zone and an α -case in the titanium matrix around the fibers,^[8] while argon cycling between 450 °C and 850 °C induced debonding around the fiber and some interfacial reaction.^[9] In summary, composite damage and concurrent degradation of properties result from fluctuations in internal stresses, which can be compounded by the oxidative degradation of the matrix and fibers in air.

The upper-use temperature of unreinforced Ti-6Al-4V is dictated by its low creep strength above about 450 °C.^[10] When reinforced, Ti-6Al-4V could be used at higher temperatures; however, embrittlement as a result of dissolution of, and reaction with, oxygen, nitrogen, and hydrogen^[11] could become a limiting factor. Nevertheless, short excursions at temperatures as high as 700 °C may be acceptable for reinforced Ti-6Al-4V because the alloy oxidation for times less than 5 to 10 hours at 700 °C is parabolic in nature, as a result of a partially protective oxide layer formed of sublayers of rutile and alumina.^[12-14] However, thermal stresses associated with the large mismatch of coefficient of thermal expansion (CTE) between matrix and reinforcement may preclude repeated excursions at high temperatures. Thus, in the present study, we investigate the behavior of SCS-6/Ti-6Al-4V composites subjected to thermal cycling between 200 °C and 700 °C in an oxidative environment. We first determine the thermally induced stresses during cooling from fabrication temperature and during thermal cycling, taking into account creep relaxation of the matrix. These results are then used to evaluate the propagation of thermal fatigue cracks, allowing

S.H. THOMIN, formerly Graduate Student, Department of Materials Science and Engineering, Massachusetts Institute of Technology, Cambridge, MA, is Ingénieur de l'Armement, Délégation Générale pour l'Armement, Centre d'Essais Aéronautique de Toulouse, 31056 Toulouse, France. P.A. NOËL, Head of the Inorganic Section, is with the New Processes and Materials Department, Matra Défense, 78140 Vélizy, France. D.C. DUNAND, Amax Assistant Professor of Materials Engineering, is with the Department of Materials Science and Engineering, Massachusetts Institute of Technology, Cambridge, MA 02139.

Manuscript submitted January 21, 1994.

identification of the relevant mechanisms for the oxidative thermal fatigue of the composite.

II. MODELING OF INTERNAL STRESSES

To evaluate the thermal stresses from CTE mismatch, we use an elastic model by Naik,^[15] considering matrix, interphase, and fiber as three coaxial, concentric cylinders, as described in Appendix A. This analytical model gives results in good agreement with more complicated finite-element models.^[15] We then incorporate into this model the temperature dependence of materials properties, since, as shown by Arnold *et al.*,^[16] large errors can result from the simplifying assumption that the materials properties are temperature independent. We consider the temperature dependence of the Young modulus $E(T)$, coefficient of thermal expansion $\alpha(T)$, and matrix yield strength $\sigma_y(T)$ (Appendix B), by averaging the stress tensor between the temperatures T_0 and T_1 as follows:

$$\bar{\sigma} = \frac{1}{T_1 - T_0} \cdot \int_{T_0}^{T_1} \bar{\sigma}[E(T), \alpha(T), \sigma_y(T)] dT \quad [1]$$

Matrix plasticity is assumed to take place when the uniaxial yield stress of the matrix is equal to the von Mises equivalent stress

$$\sigma_{eq} = \frac{\sqrt{2}}{2} [(\sigma_{rr} - \sigma_{\theta\theta})^2 + (\sigma_{rr} - \sigma_{zz})^2 + (\sigma_{\theta\theta} - \sigma_{zz})^2]^{1/2} \quad [2]$$

Because the upper temperature of the thermal cycle and the fabrication temperature in the present study are above half the absolute melting point of the matrix, matrix creep as a result of thermal stresses cannot be neglected. Multiaxial constitutive relationships^[17] are used to calculate the strain rates $\dot{\epsilon}_{ii}$ due to relaxation of matrix thermal stresses:

$$\begin{cases} \dot{\epsilon}_{rr} = \frac{1}{2} \cdot \sigma_{eq}^{n-1} \cdot (2\sigma_{rr} - \sigma_{\theta\theta} - \sigma_{zz}) \cdot A \cdot \exp\left(-\frac{Q}{RT}\right) \\ \dot{\epsilon}_{\theta\theta} = \frac{1}{2} \cdot \sigma_{eq}^{n-1} \cdot (2\sigma_{\theta\theta} - \sigma_{rr} - \sigma_{zz}) \cdot A \cdot \exp\left(-\frac{Q}{RT}\right) \\ \dot{\epsilon}_{zz} = \frac{1}{2} \cdot \sigma_{eq}^{n-1} \cdot (2\sigma_{zz} - \sigma_{\theta\theta} - \sigma_{rr}) \cdot A \cdot \exp\left(-\frac{Q}{RT}\right) \end{cases} \quad [3]$$

where the equivalent stress σ_{eq} is given by Eq. [2]. The constant A , activation energy Q , and creep exponent n correspond to those of the Norton power-law for an uniaxial stress σ as follows:

$$\dot{\epsilon} = A \cdot \sigma^n \cdot \exp(-Q/RT), \quad [4]$$

where $\dot{\epsilon}$ is the uniaxial strain rate, R is the gas constant, and T is the absolute temperature. The increment of stress $\Delta\sigma$ due to creep during time Δt is then

$$\begin{cases} \Delta\sigma_{rr} = \frac{E\nu}{(1+\nu)(1-2\nu)} \left[\frac{1-\nu}{\nu} \int_0^{\Delta t} \dot{\epsilon}_{rr} dt + \int_0^{\Delta t} \dot{\epsilon}_{\theta\theta} dt + \int_0^{\Delta t} \dot{\epsilon}_{zz} dt \right] \\ \Delta\sigma_{\theta\theta} = \frac{E\nu}{(1+\nu)(1-2\nu)} \left[\int_0^{\Delta t} \dot{\epsilon}_{rr} dt + \frac{1-\nu}{\nu} \int_0^{\Delta t} \dot{\epsilon}_{\theta\theta} dt + \int_0^{\Delta t} \dot{\epsilon}_{zz} dt \right] \\ \Delta\sigma_{zz} = \frac{E\nu}{(1+\nu)(1-2\nu)} \left[\int_0^{\Delta t} \dot{\epsilon}_{rr} dt + \int_0^{\Delta t} \dot{\epsilon}_{\theta\theta} dt + \frac{1-\nu}{\nu} \int_0^{\Delta t} \dot{\epsilon}_{zz} dt \right] \end{cases} \quad [5]$$

where ν is the matrix Poisson's ratio.

III. EXPERIMENTAL PROCEDURES

Aligned continuous silicon carbide fibers (SCS-6, fabricated by Textron Specialty Materials, Lowell, MA) were plasma-sprayed with Ti-6Al-4V to form monotapes about 250 μm in thickness. Prior to spraying, thin unalloyed titanium ribbons (1 mm in width and 25 μm in thickness, representing about 2 vol pct of the monotape) were interwoven perpendicular to the fibers at 5-mm intervals to insure fiber alignment. Six sprayed monotapes were stacked between two 110- μm -thick Ti-6Al-4V cover foils and consolidated by vacuum-hot-pressing at 940 $^\circ\text{C}$, under a residual gas pressure of less than 0.01 Pa. The resulting composite panels, containing 30 vol pct fibers, were cut with a diamond saw into rectangular samples (70 \times 10 \times 1.70 mm) with fibers parallel to the length of the sample.

These as-fabricated samples were thermally cycled between 200 $^\circ\text{C}$ and 700 $^\circ\text{C}$ in laboratory air flowing at a rate of about 170 cm^3s^{-1} , or titanium-gettered 99.998 pct argon flowing at a rate of about 17 cm^3s^{-1} . Heating of the sample was achieved with a radiant furnace (Research Incorporation Controls, Minneapolis, MN), and the temperature was controlled by a K-type thermocouple placed within a Ti-6Al-4V cylinder positioned in the heated zone. The wall thickness of the cylinder was half the composite sample thickness, thus insuring that the measured temperature corresponded to that within the composite, independently of the varying reflectivity of the Ti-6Al-4V surface. A thermal cycle consisted of a 2-minute heating period, a 1-minute plateau at 700 $^\circ\text{C}$, and a cooling period of 3 minutes (4 minutes for samples cycled in argon), without any hold at 200 $^\circ\text{C}$. Samples were subjected to a total of 500, 1250, or 2000 cycles. The same furnace was also used to age samples isothermally at 700 $^\circ\text{C}$ in flowing laboratory air for 500, 1250, or 2000 minutes.

As-fabricated and thermally exposed samples were sectioned with a low-speed diamond saw, ground with SiC paper, polished with diamond and alumina slurries, and etched for about 3 seconds in Kroll's reagent. Microhardness profiles of the matrix were measured on polished sections with a Knoop indenter under a force of 0.981 N.

The matrix of as-fabricated and thermally exposed specimens was dissolved in hydrofluoric acid and single fibers with a gage length of 10 mm were tested in tension at a cross-head speed of 17 $\mu\text{m} \cdot \text{s}^{-1}$.

Four-point bend tests were performed on composite samples at a constant crosshead speed of 45 $\mu\text{m} \cdot \text{s}^{-1}$ at

room temperature. The displacement of the tensile face at the center of the sample was measured with an extensometer with a precision of $2.5 \mu\text{m}$. The modulus of elasticity in bending E_b and the bending stress at the bottom surface of the sample σ_b were calculated from References 18 and 19, neglecting shear effects. Some cycled samples were curved after thermal cycling, probably as a result of thermal ratcheting or relaxation of residual stresses. These samples were tested with their convex face downward. The initial curvature was measured at the center of the sample and added to the displacement resulting from the mechanical test. A similar correction was performed for the stress. These corrections corresponded to 7 to 21 pct of the fracture values.

IV. RESULTS

A. Properties and Microstructure

Figure 1 shows the structure of the as-fabricated sample in a longitudinal section. Microcracks with a depth of a few microns are present on the sample surface, which consists of the rolled Ti-6Al-4V cover foil (C), showing a layer with an acicular structure, below which larger equiaxed grains are present. The sprayed Ti-6Al-4V matrix (M) consists of a mixture of fine-grained α and β phases around the fibers (F). The transverse sections of titanium ribbons (T) are also visible.

Table I lists the average mass gain Δm of the cycled and isothermally aged samples. Mass gain results from oxygen (and to a lesser extent nitrogen) absorbed by the samples, forming both a solid solution in the titanium matrix and an oxide (nitride) layer at its surface. The surface of the sample cycled 2000 times in air (Figure 2) is covered with a 15 to $20\text{-}\mu\text{m}$ -thick oxide layer (O). The matrix consists of a featureless α -case surface layer (A),

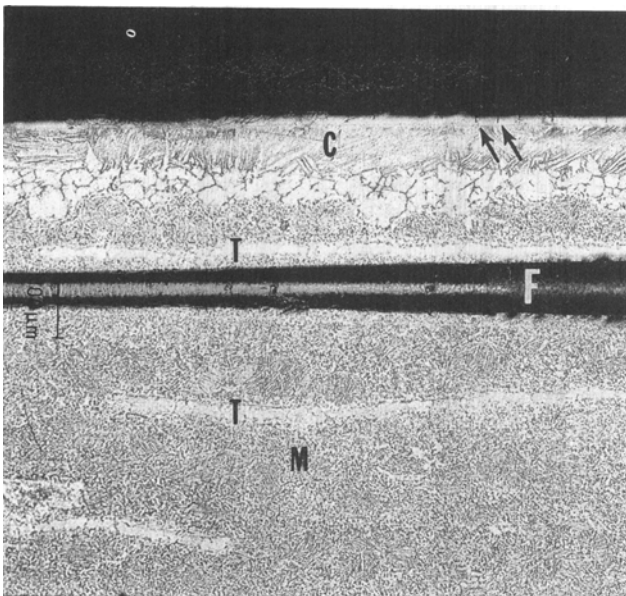


Fig. 1—Longitudinal section of an as-fabricated sample (C: Ti-6Al-4V cover foil; M: Ti-6Al-4V sprayed matrix; F: SCS-6 fiber; T: titanium ribbon). Microcracks are indicated with arrows.

about $60\text{-}\mu\text{m}$ thick, resulting from oxygen in solution within the matrix, below which coarse grains are visible. At larger depths, the matrix structure is similar to that in the as-fabricated condition. Samples cycled in argon (Figures 3 and 4) also exhibit a surface α -case, about $50\text{-}\mu\text{m}$ thick, which is covered with an oxide layer. Figure 5 gives the mean value of four measurements of Knoop microhardness as a function of distance from the surface. The peak hardness increases from about $20 \mu\text{m}$ below the surface for the as-fabricated sample, to about $40 \mu\text{m}$ for the isothermally aged sample, to about $60 \mu\text{m}$ for the air-cycled sample, indicating an increase in oxygen content with increasing exposure severity. The decrease in hardness with increasing depth after the peak value suggests that diffusion is controlling the transport of oxygen. Finally, the hardness minimum at a depth of about $110 \mu\text{m}$ corresponds to the interface between the cover foil and the sprayed matrix, the oxygen content of which is expected to be higher as a result of oxygen contamination during spraying.

Upon air exposure, the isothermally aged sample exhibits significantly smaller mass gains than the cycled samples (Table I); there is almost an order of magnitude difference in mass increase between the sample aged isothermally at 700°C for 2000 minutes (1.4 day), and the sample exposed to 2000 cycles between 200°C and 700°C , which was subjected to the same temperature of 700°C for the same amount of time (2000 minutes) as the isothermal sample. As discussed in more detail in Section V-A, the mass gain difference can be explained by the spalling of the oxide upon cycling, continuously exposing fresh metal to air. While the mass increase of the samples cycled in argon is significantly smaller than for the air-tested samples, it is nonzero and results from the small amount of oxygen present in the inert gas (20 ppm at most) flowing over the sample; after a few days of thermal cycling, the titanium getter placed ahead of the sample in the gas flow showed signs of oxidation and was replaced. The surface of the sample itself was tarnished at the end of the test, indicative of limited oxidation. The cycling experiments in argon can thus be best described as tests in a low oxygen partial pressure.

Cracks are present in all cycled samples, growing into the matrix in a plane perpendicular to the fiber axis as a result of the cyclically varying stresses generated by the CTE mismatch between fibers and matrix; these stresses are calculated in the following paragraph. Figure 2 shows for the air-cycled sample such a transverse surface crack partially filled with oxide; the cavity in the oxide within the crack was probably created during the polishing procedures, since most smaller surface cracks (Figure 6) are completely filled with oxide. The average depth of 52 transverse surface cracks measured on a specimen length of 25 mm in the sample cycled 2000 times in air is given in Table I. Figure 7 is a micrograph in the plane of a transverse crack, showing that the crack, extending to the first layer of fibers, has a complex geometry and is not entirely planar. None of the cracks, with an average width of $528 \pm 254 \mu\text{m}$, were observed to cross the whole width of the sample.

The sample cycled 1250 times in argon shows little trace of damage due to cycling (Figure 3); a few small transverse cracks containing little oxide are present on

Table I. Average Experimental Mass Gain, Crack Depth, and Crack Growth Rate for Thermally Exposed Samples

Condition	Atmosphere	Mass Gain Δm (mg · cm ⁻²)	Crack Depth a (μm)	Crack Growth Rate da/dN (μm/Cycle)
as-fabricated	—	0	5 ± 2	—
1250 cycles*	argon	0.36	53 ± 13	0.04 ± 0.01
2000 cycles*	argon	0.57	136 ± 81	0.07 ± 0.04
500 cycles*	air	9.5		
1250 cycles*	air	11		
2000 cycles*	air	20	158 ± 77	0.08 ± 0.04
2000 min**	air	2.5		

*Cycled between 200 °C and 700 °C (with a 1-min hold at 700 °C).

**Isothermally aged at 700 °C.

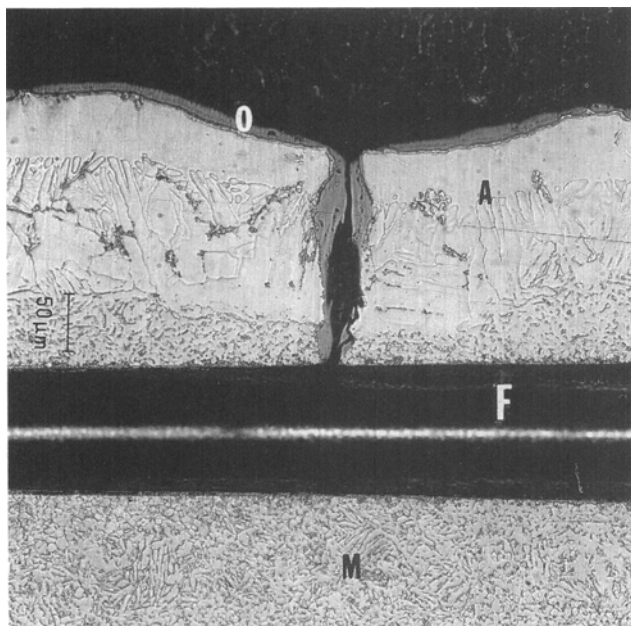


Fig. 2—Longitudinal section of a sample cycled 2000 times in air (O: surface oxide; A: α -case; F: SCS-6 fiber; M: Ti-6Al-4V sprayed matrix).

only one of the faces of the sample. Conversely, the sample cycled 2000 times in argon exhibits deeper, more numerous, partially oxidized transverse cracks, which in some cases extend to the first layer of fibers (Figure 4). Table I lists the average crack depth for these samples, measured for 10 cracks on a length of 10 mm and for 49 cracks on a length of 40 mm, respectively.

In Figure 8, the average strength of 10 to 18 fibers recovered from as-fabricated and thermally exposed samples before mechanical testing is plotted as a function of their Weibull modulus. Error bars correspond to the standard deviation for the strength and an estimated deviation of 2 for the Weibull modulus. Fibers from the first layer (closest to the specimen surface), second layer, and third layer (at the center of the specimen) are shown with different symbols. First-layer fibers of the sample cycled 2000 times in air were too brittle to be tested because of direct contact with air from the deep surface cracks extending to the first fiber layer (Figure 2). While the average strength of the tested fibers is not significantly different, the Weibull modulus

decreases with increasing cycle number, decreasing depth from the surface, and increasing severity of the environment, indicating that the fibers are damaged by the oxygen diffusing from the surface or transported through cracks.

The same trend is observed in Figure 9 for the composite bending fracture stress, σ_{bf} , decreasing with increasing cycle number and increasing environment severity, reflecting the damage in the matrix (cracks and brittle α -case) and the fibers (reduced Weibull modulus). The bending modulus is virtually unchanged up to 1250 cycles, but decreases significantly after 2000 cycles (Figure 10); as expected, the decrease is more rapid in air than in argon.

The tension edge of fractured samples is shown in Figures 11 and 12. The as-fabricated sample (Figure 11) exhibits fiber pullout and a matrix with numerous dimples, indicative of local ductility. The same type of features are present on the fractured edges of isothermally aged samples. However, the sample cycled 2000 times in air (Figure 12) shows little fiber pullout and a cleaved fracture surface typical of brittle fracture, as expected from the α -case at the surface. Oxide on one of the faces of a crack is also visible on this micrograph as a darker scale (O), indicating that fracture probably initiated from oxidized cracks.

B. Stress Computations

Figures 13 and 14 show the maximum values (at the interface between the Ti-6Al-4V matrix and the TiC interphase) of the matrix principal stresses and equivalent stress upon cooling from processing temperature to room temperature, calculated from Eqs. [A2], [A3], [A6], and [A8] (Appendix A) for the experimental cooling rate of 225 K · h⁻¹. Equations [1] and [5], which take into account matrix deformation by creep and the temperature-dependent materials properties given in Appendix B, are treated under isothermal conditions using finite differences with steps of 1 K and about 0.1 s, respectively. Taking into account matrix creep, the magnitude of the maximum equivalent stress generated during cooling increases from 0 MPa at 940 °C to about 400 MPa at room temperature. The matrix equivalent stress does not reach the matrix yield stress at any point during cooling and the elastic analysis described in Appendix A can thus be used at all temperatures. If creep is not taken into account, however,

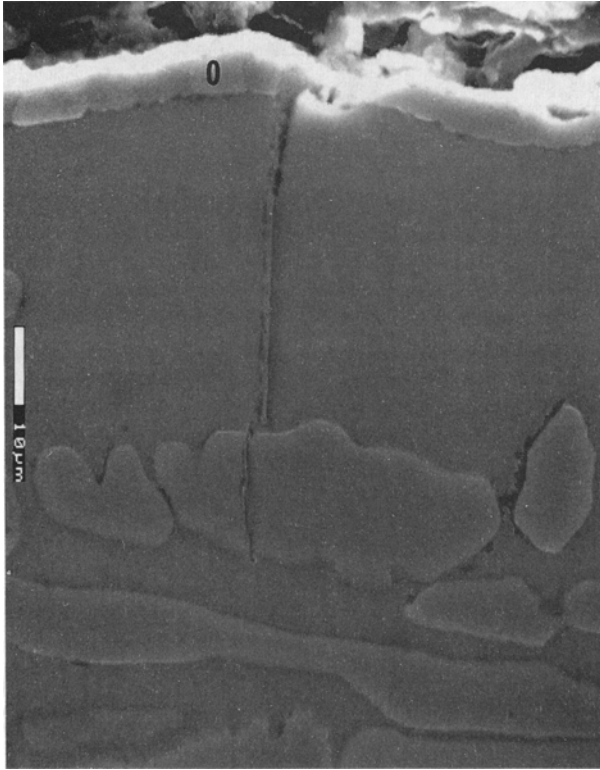


Fig. 3—Longitudinal section of oxidized transverse surface crack in a sample cycled 1250 times in argon (O: surface oxide).

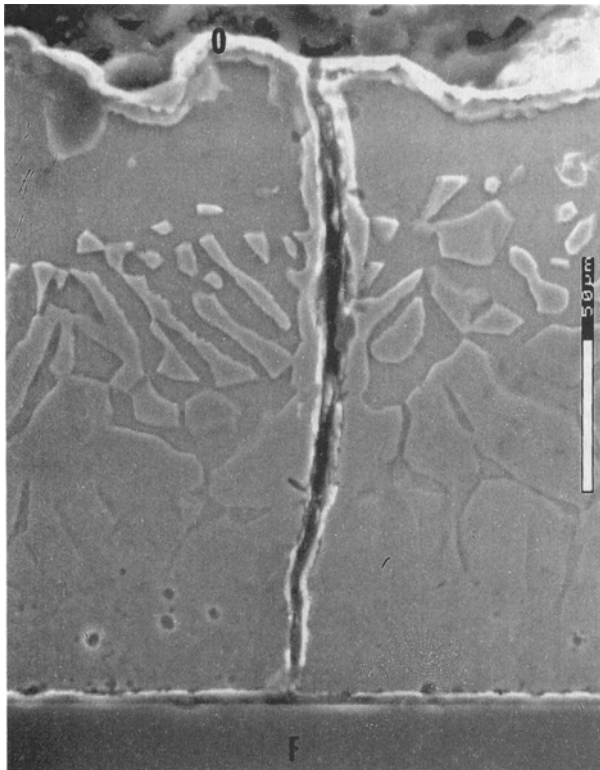


Fig. 4—Longitudinal section of oxidized transverse surface crack in a sample cycled 2000 times in argon (O: surface oxide; F: fiber).

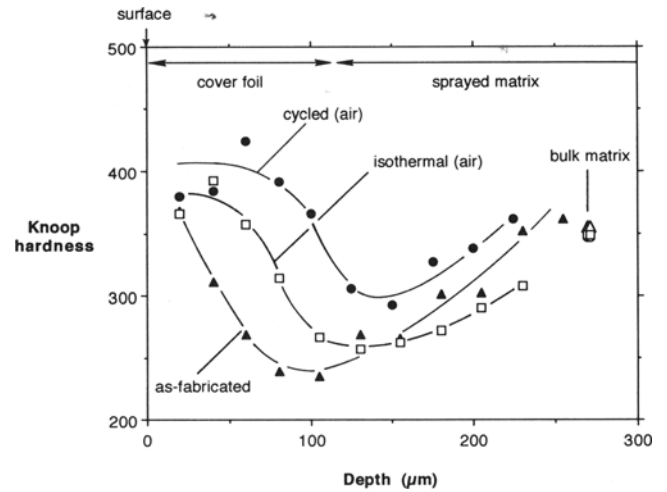


Fig. 5—Knoop microhardness as a function of distance from the sample surface for an as-fabricated sample, an isothermally air-aged sample (2000 min) and an air-cycled sample (2000 cycles).

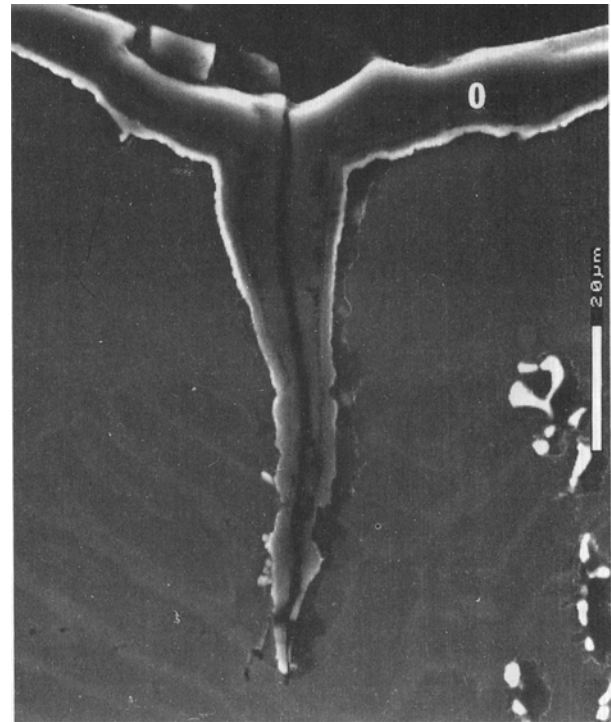


Fig. 6—Longitudinal section of oxidized surface transverse crack in a sample cycled 2000 times in air (O: surface oxide).

plastic yielding is predicted to occur during cooling at elevated temperature, leading to a room-temperature equivalent stress with a value intermediate between that of the purely elastic solution and the elastic-creeping solution shown in Figure 14.

The materials parameters used for creep in Eq. [4] ($Q = 188 \text{ kJ} \cdot \text{mol}^{-1}$, $n = 2.8$ and $A = 1.88 \cdot 10^{-17}$) were derived from data measured on Ti-6Al-4V between 450 °C and 600 °C by Sastry *et al.*^[20] and were assumed to be valid up to 940 °C. Therefore, the present calculation is approximate between 600 °C and 940 °C, since

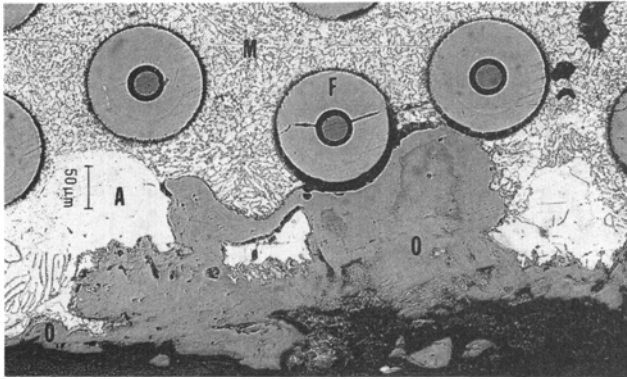


Fig. 7—Transverse section of an oxidized transverse surface crack in a sample cycled 2000 times in air (O: surface oxide; A: α -case). Split fiber (F) is most probably a preparation artifact.

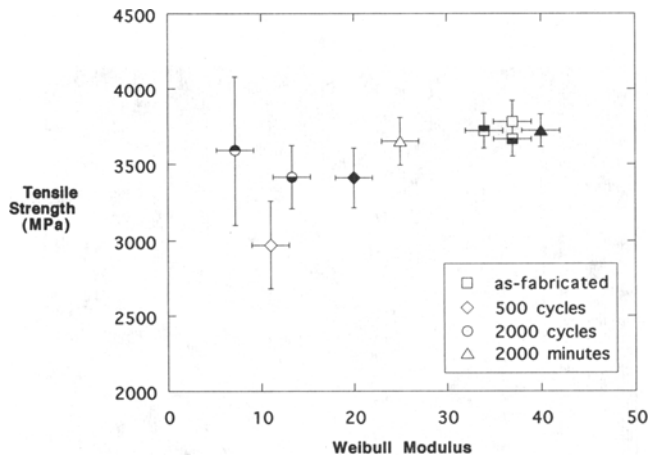


Fig. 8—Plot of average fracture strength and Weibull modulus of individual fibers extracted from samples isothermally aged in air or cycled in air. Empty symbols: first layer of fibers; symbols with filled upper half: second layer of fibers; symbols with filled lower half: third layer of fibers; filled symbols: both second and third layers of fibers.

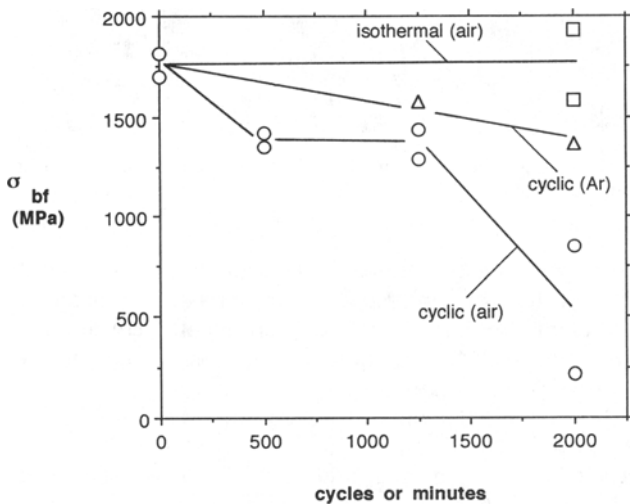


Fig. 9—Fracture bending stress σ_{bf} as a function of the number of cycles or minutes at 700 °C.

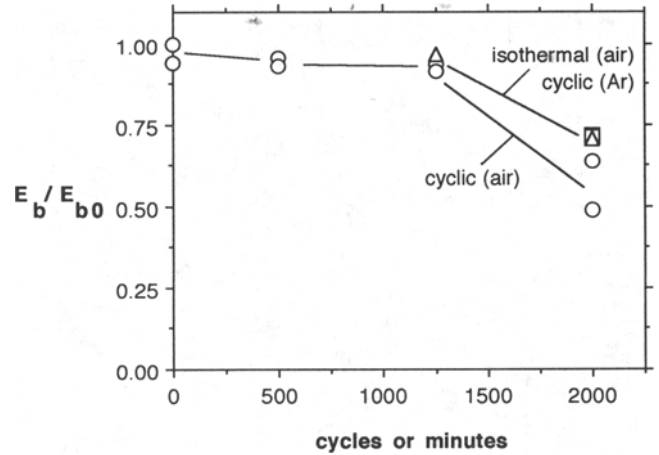


Fig. 10—Bending modulus E_b (normalized by that of the as-fabricated sample E_{b0}) as a function of the number of cycles or minutes at 700 °C.

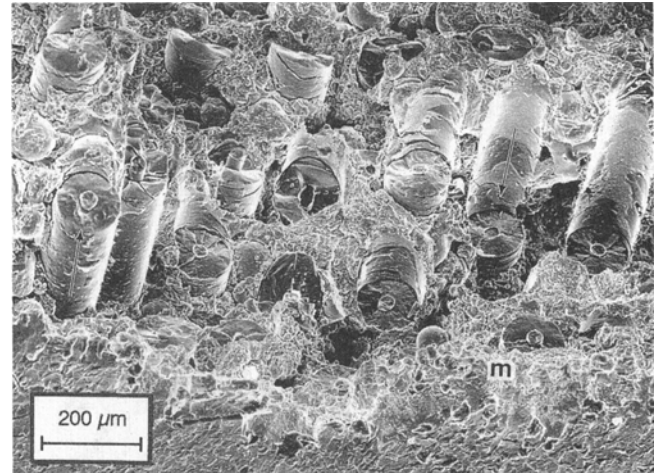


Fig. 11—Tensile fractured edge of an as-fabricated sample (arrow: fiber pullout; M: matrix).

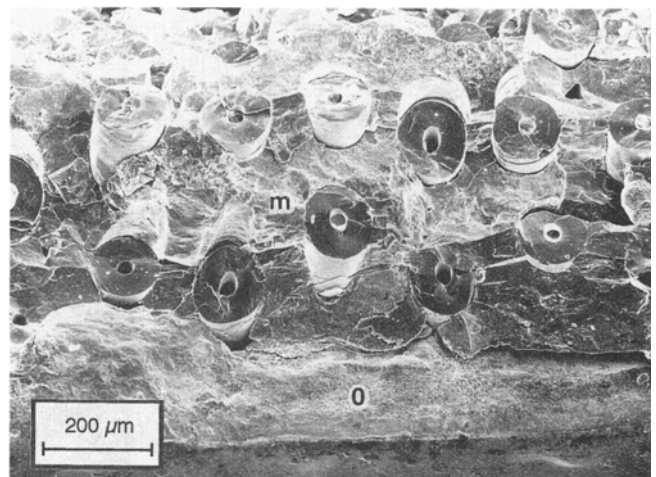


Fig. 12—Tensile fractured edge of a sample cycled 2000 times in air (O: crack oxide; M: matrix).

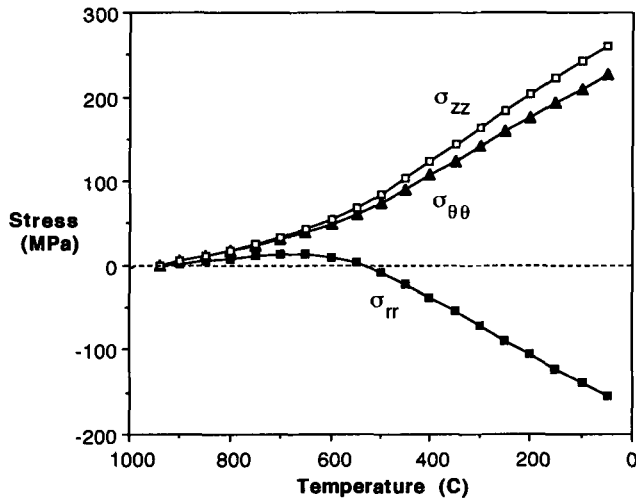


Fig. 13—Maximum principal matrix stresses during cooling from processing temperature, with creeping matrix and temperature-dependent materials properties.

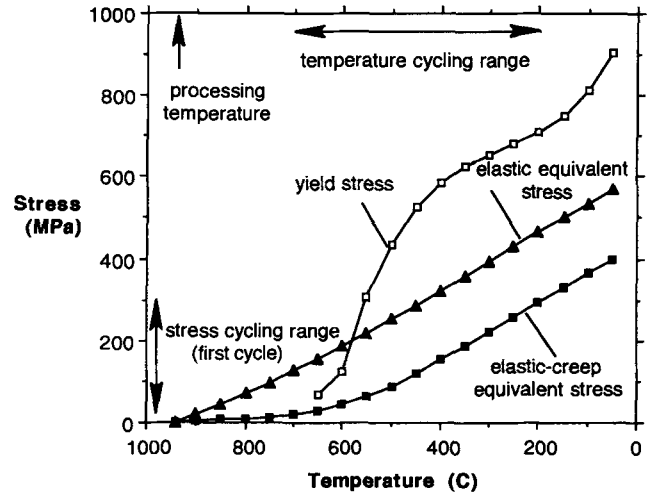


Fig. 14—Yield strength, maximum elastic equivalent stress (without matrix creep), and maximum equivalent stress (with matrix creep, from Fig. 13) in the matrix as a function of temperature during cooling from processing temperature.

factors such as superplastic deformation and varying amounts of α and β phases are likely to alter the creep behavior of Ti-6Al-4V in this temperature range. Furthermore, Eq. [4] only considers steady-state secondary creep and thus may underestimate the actual creep strain, which also includes the contribution of primary creep. However, the absolute error in the residual stress at room temperature is likely to be small, since the matrix stresses at elevated temperature are low.

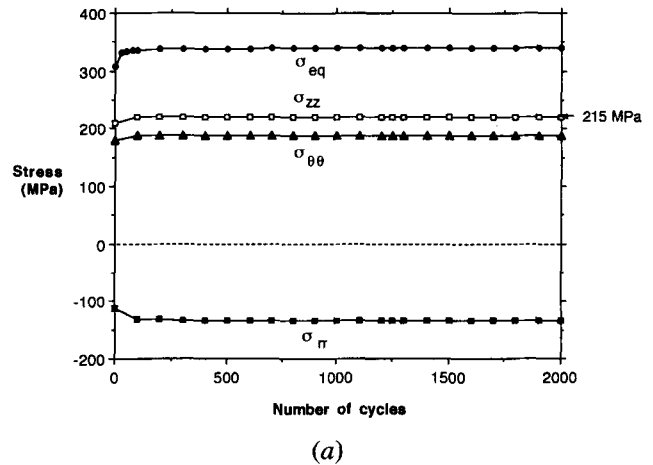
From the state of stress at room temperature (Figures 13 and 14), the principal stresses (Appendix B), and the equivalent stress (Eq. [2]) in the matrix at the upper and lower temperature of the cycle are determined as a function of the number of cycles for the experimental temperature cycle described previously and assuming matrix creep. As shown in Figures 15(a) and (b), the maximum value of the equivalent stress never exceeds the matrix yield stress during thermal cycling, allowing the use of the elastic analysis described previously for the whole temperature cycle. Due to creep at high temperature, the principal and equivalent matrix stresses, the maximum value of which is given in Figures 15(a) and (b), vary during the first 250 cycles to then become nearly constant.

V. DISCUSSION

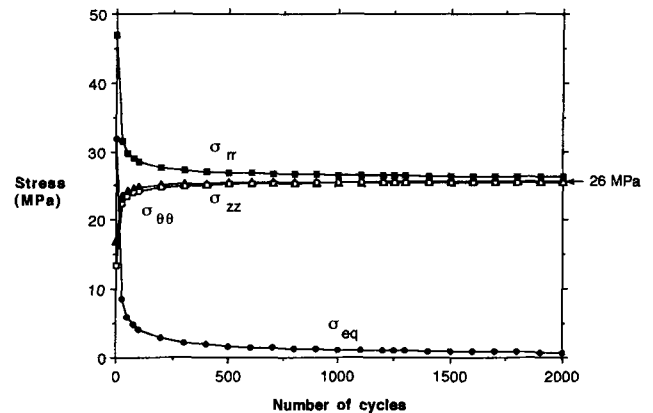
A. Oxidation

1. Matrix oxidation

The average mass increase of $2.5 \text{ mg} \cdot \text{cm}^{-2}$ for the samples isothermally aged for 2000 minutes at 700°C (Table 1) is in reasonable agreement with the value of about $1.7 \text{ mg} \cdot \text{cm}^{-2}$ reported by Champin *et al.*^[12] for the oxidation of bulk Ti-6Al-4V under the same conditions. For both isothermally aged and as-fabricated samples, the appearance of the fractured matrix after mechanical testing and the hardness of the matrix about $125 \mu\text{m}$ below the surface are similar (Figure 5). Also, the strength (Figure 9) is virtually unchanged after aging. These observations indicate that these composites



(a)



(b)

Fig. 15—Matrix maximum principal stress and maximum equivalent stress (with creep relaxation of the matrix) at (a) 200°C and (b) 700°C as a function of the number of cycles.

are oxidized at the surface only, without significant degradation of the bulk matrix microstructure or mechanical properties.

The important mass increase after thermal cycling in air—almost ten times that of isothermally aged samples in air—indicates that a large quantity of oxygen was incorporated into the samples during cycling, both as oxygen in solid solution within the matrix bulk and as oxide at the sample surface. The increase of surface exposed to oxidation due to the formation of transverse cracks in these samples is, however, less than 4 pct and cannot account for the observed mass increase. Rather, the cyclic thermal stresses seem responsible for the increased oxidation. A similar trend was reported for unreinforced Ti-6Al-4V samples cycled between room temperature and 650 °C,^[12] which exhibited twice the mass increase of isothermally aged Ti-6Al-4V samples. For unreinforced Ti-6Al-4V, compressive thermal stresses are generated in the oxide scale by the CTE difference between the alloy ($\alpha_m = 10.7 \cdot 10^{-6} \text{ K}^{-1}$ between 25 °C and 700 °C^[21]) and the oxides forming the scale ($\alpha_{\text{TiO}_2} = 7.8 \cdot 10^{-6} \text{ K}^{-1}$ between 20 °C and 600 °C and $\alpha_{\text{Al}_2\text{O}_3} = 7.83 \cdot 10^{-6} \text{ K}^{-1}$ between 0 °C and 727 °C^[22]), growing at the upper temperature of the cycle. Compressive fracture of the oxide scale thus takes place upon cooling,^[13] allowing access of oxygen to the underlying metal and oxidation during the subsequent cycle.

The much higher oxidation observed for the cycled composite can be attributed to the low CTE of the composite, calculated to be $6.1 \cdot 10^{-6} \text{ K}^{-1}$, using Shapery's approximation for the axial coefficient of thermal expansion of an unidirectional continuously reinforced composite:^[23]

$$\alpha_c = \frac{E_m v_m \alpha_m + E_f v_f \alpha_f}{E_m v_m + E_f v_f} \quad [6]$$

where v is the volume fraction, and the average CTE of the SCS-6 fibers is $\alpha_f = 3.9 \cdot 10^{-6} \text{ K}^{-1}$ between 25 °C and 700 °C^[16]. Since, unlike the unreinforced alloy, the CTE of the composite is lower than that of the oxide, tensile stresses build up in the oxide upon cooling from the elevated temperature at which it is formed. These tensile residual stresses are more likely to induce cracks in the brittle oxide than the compressive stresses in the case of the unreinforced material, explaining the higher mass gains of the cycled composite. Finally, since the mass gain of the samples cycled in argon is even less than that of the isothermally aged samples, it can be concluded that both thermal stresses and high oxygen concentrations are responsible for the large mass increase of the air-cycled samples.

2. Fiber oxidation

As expected, the properties of the fibers in the as-fabricated sample do not vary with their position with respect to the surface: fibers from the first layer (closest to the specimen surface), second layer, and third layer (at the center of the specimen) show similar strength and Weibull modulus (Figure 8). The sample isothermally aged in air for 2000 minutes shows fibers with an average strength similar to those of the as-fabricated sample but a lower Weibull modulus in the first layer, indicating that some damage has taken place. This result

is in agreement with the composite mechanical properties (Figures 9 and 10); the strength of the air-aged sample is the same as that of the as-fabricated sample, but the bending modulus is lower, probably as a result of early fracture of the fibers at the lower end of the strength distribution. Fiber degradation can be explained by bulk diffusion of oxygen from the surface (Figure 5) and subsequent reaction of oxygen with the carbon-rich layer present at the surface of SCS-6 fibers.^[24]

For the sample cycled 500 times in air, the fibers in the first layer exhibit significantly lower Weibull modulus and strength than the fibers in the deeper layers (2 and 3), the strength and Weibull modulus of which are in turn lower than those of the as-fabricated or isothermally aged fibers. This trend is confirmed by the low properties of the fibers for the sample air-cycled 2000 times; the fibers in the first layer are too brittle to be tested, while the Weibull modulus of the inside layers is significantly lower than for the sample air-cycled 500 times. The decrease in composite strength measured with increasing cycling time (Figure 9) and the degradation of fiber properties with increasing cycling time and decreasing depth from the surface (Figure 8) thus indicate that fiber oxidation is controlled by the cracks (Figures 2, 3, 4, 6, and 7) which give direct access to oxygen to the first layer of fibers and reduce the diffusion distance for the deeper layers. In what follows, we examine the mechanisms responsible for matrix cracking in the cycled composites.

B. Thermal Fatigue

Figure 14 shows the importance of taking into account matrix creep upon cooling from the processing temperature: the purely elastic analysis overestimates the peak residual stresses after cooling, even if plasticity is considered. A precise knowledge of these residual stresses is important, since they determine the range of stresses between which the matrix is cycled upon subsequent thermal cycling (Figure 15), which in turn controls the thermal fatigue behavior of the matrix. Comparison of the equivalent stress curves with and without matrix creep in Figure 14 shows that the relaxation effect of creep is gradual and spread over a large temperature range (between 940 °C and about 550 °C). We do not attempt to quantitatively compare Figure 14 with residual stresses calculated by finite elements in SCS-6-reinforced Ti-6-4 by Nimmer *et al.*^[25] and Durodola and Derby^[26] because the materials constants (elastic, plastic, and thermal properties) and the experimental conditions (fiber volume fraction, stress-free temperature, and cooling rate) are somewhat different. The preceding authors, however, report significant reductions of residual stresses when matrix creep is taken into account, in qualitative agreement with results shown in Figure 14.

As is the case during cooling, the equivalent stress does not reach the plastic limit at any time during thermal cycling. Figure 15(b) shows that creep during the first few hundreds 1-minute hold periods at 700 °C brings the peak equivalent stress to a value near zero, while the peak principal stresses stabilize to a nonzero, constant value of about 26 MPa. Without relaxation of the fibers, which are assumed to be noncreeping, this

matrix hydrostatic residual stress cannot be relaxed to zero. As a result of stress relaxation at elevated temperature, whereby the radial stress decreases but the hoop and axial stress increase (Figure 15(b)), the three principal stresses and the equivalent stress are enhanced at the low temperature of the cycle (Figure 15(a)). These stresses, however, are stabilized after about 100 cycles.

Air-cycled samples exhibit extensive microstructural damage in the form of numerous transverse cracks (Figures 2 and 6). At low temperatures, where internal stresses are high and crack growth is expected, the radial stresses in the matrix are compressive; hence, only hoop and axial stresses are considered for thermal fatigue. Because tensile axial stresses are larger than hoop stresses, transverse cracks are expected to be more numerous and larger than radial cracks, as indeed observed experimentally in the microstructural investigation.

We first examine the effect of thermal fatigue on the propagation of transverse cracks in the matrix without the embrittling effect of oxygen. We ignore the contribution of the hoop stress, which does not open the transverse cracks. We assume that the axial stress, which is independent of the radial distance from the fiber as a result of the generalized plane strain condition in the composite (Appendix A), is given by the model derived above for the whole matrix in the composite, including the Ti-6Al-4V cover foil. We note that the latter assumption was verified in only one of the two composite systems investigated by Cox *et al.*^[27] and is thus not always valid.

We assume that we can use the mode I stress intensity factor range ΔK for an edge-cracked semi-infinite plate containing a crack of length a :^[28]

$$\Delta K = 1.122 \cdot (\sigma_{\max} - \sigma_{\min}) \cdot \sqrt{\pi \cdot a} \quad [7]$$

cycled between a maximum tensile stress $\sigma_{\max} = 215$ MPa and a minimum tensile stress $\sigma_{\min} = 26$ MPa, which are the axial stresses at 200 °C and 700 °C, respectively (Figure 15). If the initial 5- μm depth of the microcracks found on the surface of the as-fabricated sample (Figure 1) is taken for the crack depth a , Eq. [7] yields $\Delta K = 0.84$ MPa \cdot m^{1/2}. This value is smaller than the minimum value ($\Delta K = 2$ MPa \cdot m^{1/2}) investigated by Wagner and Lütjering^[29] for the growth of short surface cracks in Ti-6Al-4V. The crack growth rate extrapolated from the preceding reference for $\Delta K = 0.84$ MPa \cdot m^{1/2} is $da/dN = 0.1$ to 1 nm/cycle, much smaller than the observed average crack growth rate in air or argon $da/dN = 40$ to 80 nm/cycle (Table I). Even if we set a to the average final length of the cracks found in the sample cycled in air 2000 times ($a = 158$ μm), the stress intensity factor range becomes $\Delta K = 4.7$ MPa \cdot m^{1/2} and the crack growth rate according to Wagner and Lütjering^[29] is $da/dN = 4$ to 20 nm/cycle, still too low to account for the observed depth of the cracks. The effects of temperature and moisture in our experiments do not explain the discrepancy: Wei and Ritter^[30] found that fatigue crack growth of mill-annealed Ti-6Al-4V is virtually independent of temperature between 25 °C and 290 °C and only weakly sensitive to moisture at levels as low as 30 ppm. Thus, despite the many simplifying assumptions made previously, the large discrepancy between calculated and observed crack propagation rates

shows that thermal fatigue alone cannot explain the deep cracks found in the cycled samples. We now examine other possible mechanisms that can enhance thermal fatigue of the composites.

C. Oxygen Embrittlement

The fracture toughness and fatigue resistance of Ti-6Al-4V decrease with increasing oxygen content.^[31] Titanium ductility also decreases sharply with increasing oxygen content to a value near zero for 0.75 at. pct oxygen.^[11] Oxygen can penetrate into the matrix in two ways:

- (1) Bulk diffusion from the surface of the sample, embrittling the whole matrix.
- (2) Diffusion at the crack tip resulting in local embrittlement of the matrix.^[32]

We assume that both phenomena can be approximated by the diffusion equation in a semi-infinite medium. The concentration of oxygen c at distance x from the surface at time t is then given by the following:

$$c(x) = c_0 \cdot \operatorname{erfc} \left(\frac{x}{2\sqrt{Dt}} \right) \quad [8]$$

where D is the diffusion coefficient of oxygen in the metal, c_0 is the oxygen concentration at the gas/surface interface and the concentration at $t = 0$ is nil for $x > 0$. Because the coefficient of diffusion of oxygen in titanium D is a strong function of the temperature, we assume that diffusion of oxygen occurs only during the 1-minute hold at the maximum temperature of the cycles (700 °C) and neglect diffusion during the rapid heating or cooling periods of the cycle.

We first examine bulk diffusion (mechanism (1)). As seen from the microhardness measurements in Figure 5, which can be correlated to oxygen content,^[33] oxygen concentration increases in order from the as-fabricated sample, to the isothermally air-aged sample, to the air-cycled sample. While the total exposure time at 700 °C is the same for the latter two samples, the observed difference in oxygen content is probably the result of the tensile thermal stresses cracking the oxide layer in the cycled sample, as discussed previously. Therefore, oxygen is in contact with fresh metal without first having to diffuse through the partially protective oxide layers.^[34]

We assume that matrix embrittlement by dissolution of oxygen takes place at concentrations above 0.75 at. pct O, as observed in unalloyed titanium,^[11] and that the diffusion coefficient of oxygen in titanium can be used for Ti-6Al-4V. Equation [8] with $c_0 = 32$ at. pct^[35] and $D = 1.1 \cdot 10^{-15}$ m² \cdot s⁻¹^[34] gives $x = 32$ μm ($t = 1250$ min) and $x = 40$ μm ($t = 2000$ min) for the depth at which the oxygen concentration is $c = 0.75$ at. pct. These diffusion distances are in reasonable agreement with the observed depth of the α -case of all cycled samples but are significantly less than the observed average crack depth $x = 53$ μm (1250 cycles) and $x = 147$ μm (2000 cycles). We thus conclude that embrittlement of the metal by volume diffusion of oxygen from the surface does not explain the observed depth of cracks in the cycled samples.

We now consider the diffusion at the crack tip (mechanism (2)). This mechanism, also proposed by Revelos and Smith^[4] for crack propagation in air-cycled titanium aluminide composites, takes place according to the following steps: (a) during the 1-minute hold at high temperature, oxygen diffuses into the matrix at the crack tip; and (b) upon cooling, matrix tensile axial stresses increase and the crack propagates in the embrittled matrix, exposing uncontaminated material to oxygen upon heating in the next cycle. Crack propagation by creep at the maximum temperature is neglected, since thermal stresses are low at 700 °C (Figure 15(b)).

We assume that for each cycle, the crack propagates at the crack tip in the oxygen-embrittled zone containing oxygen in solid solution by a distance $\lambda = da/dN \cdot 1 = 80$ nm, the maximum experimental value for the sample cycled 2000 times in air (Table I). Assuming again that $c_o = 32$ at. pct at the crack tip, Eq. [8] yields an oxygen concentration at a distance λ from the crack tip after one minute of diffusion at 700 °C of $c = 27$ at. pct, much higher than the critical concentration for embrittlement of 0.75 at. pct. For this critical concentration to be found at the distance λ from the crack tip, a small value of $c_o = 0.9$ at. pct (Eq. [8]) is necessary. This oxygen concentration is most likely exceeded at the tip of the crack, since oxide is found within the whole crack. We thus conclude that crack tip embrittlement is a possible mechanism for the observed average crack propagation rate.

We note that oxide formation at the crack tip may also lead to further embrittlement and acceleration of crack growth. The mechanism is similar to that described previously for embrittlement by oxygen diffusion, except that the embrittled region is formed of oxide at the crack tip and a solid solution of oxygen in titanium at larger distances from the tip. As shown previously, the embrittlement by oxygen alloying alone, however, is sufficient to explain the observed crack growth rates.

D. Crack Wedging by Oxide

For the majority of the cracks in the air-cycled specimens, the oxide layer within the cracks is thicker near the surface than close to the crack tip, leading to a triangular shape in longitudinal metallographic sections (Figure 6). This confirms that cracks nucleated at the surface and extended inward, not the opposite.

When titanium (density $\rho = 4500 \text{ kg} \cdot \text{m}^{-3}$) oxidizes to rutile (density $\rho = 4250 \text{ kg} \cdot \text{m}^{-3}$), there is an increase in volume by a factor k :^[36]

$$k = \frac{M_{\text{TiO}_2}}{M_{\text{Ti}}} \cdot \frac{\rho_{\text{Ti}}}{\rho_{\text{TiO}_2}} \quad [9]$$

where M is the atomic or molecular mass. For the system Ti-TiO₂, Eq. [9] yields $k = 1.76$, *i.e.*, 1 m³ of titanium is replaced by 1.76 m³ of rutile. If it is not extruded out of the crack, this excess oxide opens the faces of the crack like an expanding wedge, as proposed by Smith and Marder^[37] for cracks containing sulfide corrosion products in a steel subjected to thermal fatigue. The mechanism is different from oxide-induced crack closure,^[36,38] whereby oxide with a thickness similar to the crack tip opening displacement retards crack growth by

closing the crack and reducing the crack tip stress intensity. Since the large amount of oxide found in the cracks is not extruded in our samples (Figures 2, 3, 4, 6, and 7), we estimate the magnitude of crack wedging in what follows, with many simplifying assumptions.

We neglect the stresses from CTE mismatch between oxide and matrix,^[39] since the volume mismatch (Eq. [9]) is many orders of magnitude larger than the CTE mismatch. Assuming that the volume increase is entirely used to open the crack in the longitudinal z direction and that the oxide is incompressible, the crack opening displacement Δ due to the excess volume is the difference between the observed distance d' between the two faces of the crack containing the oxide, and the distance between the faces of crack $d = d'/k$ if the oxide is removed (Figure 16):

$$\Delta = d' (1 - k^{-1}) \quad [10]$$

The stress intensity resulting from the oxide wedge opening the crack by an amount Δ is assumed to be equal to the stress intensity from a far-field stress σ , inducing the same crack opening displacement Δ , for which we can use the expression^[40]

$$\Delta = \frac{4\sigma}{E} (a + r_p) \quad [11]$$

where r_p is the extent of the plastic zone, E is the elastic modulus, and the stress σ is related to the stress intensity factor K by

$$K = \alpha\sigma\sqrt{\pi a} \quad [12]$$

where α is a geometrical factor.

Equation [11] is valid for a crack with walls displaced according to a parabolic law between Δ at the mouth of the crack and δ (crack tip opening displacement) at the tip of the crack. Equation [11] is thus not strictly equal to Eq. [10], where the faces of the crack are assumed planar. The extent of the plastic zone at the tip of the crack, r_p , is as follows for plane-strain conditions:^[36]

$$r_p = \frac{K^2}{3\pi\sigma_y^2} \quad [13]$$

where σ_y is the yield stress.

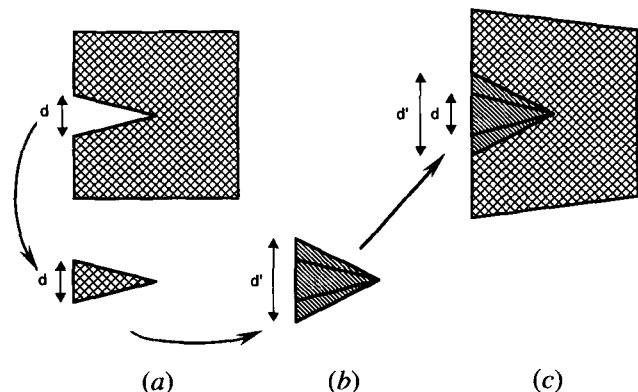


Fig. 16—Schematic of wedging action of oxide: (a) a wedge of metal is removed from the sample leaving a crack of height d ; (b) the metal wedge is oxidized to an oxide wedge with height d' ; and (c) the oxide wedge is replaced in the sample, opening the crack by an amount $\Delta = d' - d$.

Combining Eqs. [10] through [13] and eliminating the parameters Δ , σ , and r_p yields a simple implicit equation for K as follows:

$$K^3 + 3\pi\alpha\sigma_y^2 K - \frac{3}{4}\pi\sigma_y^2\alpha E\sqrt{\pi ad'}(1 - k^{-1}) = 0 \quad [14]$$

containing the experimentally observable parameters a and d' , the geometrical constant $\alpha = 1.122$, and the materials constants $k = 1.76$, $E = 96$ GPa, and $\sigma_y = 710$ MPa (for Ti-6Al-4V at 200 °C^[10]). For example, for the crack of Figure 6 ($a \approx 83$ μm and $d' \approx 22$ μm), Eq. [14] yields a value $K \approx 22$ MPa \cdot m^{1/2}. For Figure 3 ($a \approx 70$ μm and $d' \approx 2$ μm) and Figure 4 ($a \approx 212$ μm and $d' \approx 15$ μm), the values for the stress intensity predicted by Eq. [14] are $K \approx 5$ MPa \cdot m^{1/2} and $K \approx 17$ MPa \cdot m^{1/2}, respectively. These static values are significantly larger than the cyclic stress intensity due to the thermal stresses calculated previously.

For the cracks of Figures 3, 4, 6, and 7, which are representative of the cracks found in their respective samples, the estimated stress intensities due to the oxide wedging are less than the fracture toughness of equiaxed Ti-6Al-4V ($K_{IC} = 44$ to 66 MPa \cdot m^{1/2} at room temperature^[31]). However, static fracture may occur in the oxygen-embrittled zone ahead of the crack if the critical stress intensity is lowered by oxygen alloying^[31] below the values of stress intensity calculated above. Furthermore, application of a far-field stress under cyclic loading conditions increases the load ratio and also accelerates fatigue crack propagation in Ti-6Al-4V.^[31] Since the effect of crack wedging becomes negligible for small cracks containing little oxide (for a and d' tending to zero, K tends to zero in Eq. [14]), the preceding mechanism can be expected to be important only for cracks that have a significant depth and oxide content. Crack wedging thus does not explain the early stage of cracks growth in the composite, for which oxygen embrittlement and cyclical internal stresses are the determining mechanisms.

VI. SUMMARY

Continuously reinforced SCS-6/Ti-6Al-4V composites were cycled up to 2000 times between 200 °C and 700 °C or isothermally aged at 700 °C for up to 2000 minutes, in either laboratory air or argon with small amounts of oxygen. For samples cycled in air, bending modulus and bending fracture stress exhibit a sharp decrease with an increasing number of cycles. This trend is not as pronounced for the samples cycled in argon, while the isothermally treated specimens show almost no difference when compared to as-fabricated samples, except for a drop in modulus after 2000 min at 700 °C.

Deterioration of mechanical properties is correlated to microstructural damage in the form of surface transverse cracks—observed to form at the surface and propagate into the matrix perpendicularly to the fiber direction—and subsequent fiber oxidation. These cracks grow as a result of cyclically varying stresses due to the mismatch of thermal expansion between fibers and matrix. These elastic stresses are calculated using a three-dimensional

analytical model taking into account relaxation by matrix creep and the temperature dependence of materials properties. Matrix creep during cooling from processing temperature and during thermal cycling significantly alters the stress state of the matrix, which does not reach the plastic limit at any time during the experiments. Fatigue from these thermal stresses cannot, however, solely account for the rapid propagation of matrix cracks: the presence of oxygen, even in small amounts in argon, is further needed to explain the growth rate of these cracks in the thermally cycled samples. Oxygen may embrittle the crack tip by rapid diffusion during the high-temperature part of the cycle, resulting in crack propagation during the low-temperature part of the cycle, for which the thermal stresses are maximum. Furthermore, crack wedging, as the result of oxide formation within the cracks, results in tensile stresses opening the crack faces and possibly accelerating their growth. A simple derivation of the stress intensity from crack wedging is given.

In conclusion, both thermally induced cyclical stresses and the presence of oxygen, embrittling, and oxidizing the matrix are needed to propagate cracks in the matrix. These cracks lead to a deterioration of the composite mechanical properties (a) by mechanically weakening the matrix and (b) by allowing oxygen to oxidize and degrade the fibers.

APPENDIX A

Elastic three-cylinder model

The three-cylinder model by Naik^[15] is summarized in what follows. The model describes the elastic stresses in an isothermal, continuous, uniaxial composite formed of three phases (matrix, fiber, and interphase layer) with the following assumptions:

- (1) A single fiber and its surrounding interphase and matrix are representative of the whole composite.
- (2) The phases are represented by three homogeneous, isotropic, elastic, perfectly bonded, concentric cylinders (Figure A1).
- (3) Axisymmetry is imposed for the stresses and the displacements in all cylinders.
- (4) A state of generalized plane strain exists in the fiber axial direction, *i.e.*, the axial stress and strain are constant in each of the three regions.

The equation of equilibrium for the three cylinders (Figure A1) under thermal stresses is

$$\nabla \cdot \bar{\sigma} = 0, \quad [A1]$$

for which the general solution for the in-plane stresses of the stress tensor $\bar{\sigma}$ in cylindrical coordinates is^[41]

$$\sigma_{rr,i}(r) = a_i - \frac{b_i}{r^2} \quad [A2a]$$

$$\sigma_{\theta\theta,i}(r) = a_i + \frac{b_i}{r^2} \quad [A2b]$$

where a and b are constants and the subscript i denotes one of the phases (fiber f , interfacial layer l , or matrix m). In the cylindrical coordinate frame of Figure A1, the

shear stresses are negligible far from the ends of the cylinder;^[42] hence, the stress and strain tensors are reduced to diagonal matrices.

The outer radius of the matrix cylinder (R_m) is chosen to achieve the appropriate average fiber volume fraction (V_f) of the samples: $V_f = (R_f/R_m)^2$, where R_f is the radius of the fiber. The outer radius of the interphase layer R_l is set according to experimental measurements. Only two unknown constants, e.g., a_l and b_l , are needed to describe in-plane stresses in the three cylinders, due to the following continuity conditions:

$$\sigma_{rr,f} = \sigma_{\theta\theta,f} = a_f \quad \text{at } r = 0, \quad [\text{A3a}]$$

$$\sigma_{rr,f} = \sigma_{rr,l} \quad \text{at } r = R_f, \quad [\text{A3b}]$$

$$\sigma_{rr,l} = \sigma_{rr,m} \quad \text{at } r = R_l, \quad [\text{A3c}]$$

$$\sigma_{rr,m} = 0 \quad \text{at } r = R_m \quad [\text{A3d}]$$

For each phase, the strains $\varepsilon_{\theta\theta}$ and ε_{zz} are

$$\begin{aligned} \varepsilon_{\theta\theta,i}(r) = \frac{1}{E} & (-\nu\sigma_{rr,i}(r) + \sigma_{\theta\theta,i}(r) - \nu\sigma_{zz,i}) \\ & + \alpha\Delta T \end{aligned} \quad [\text{A4a}]$$

$$\begin{aligned} \varepsilon_{zz,i} = \varepsilon_a = \frac{1}{E} & (-\nu\sigma_{rr,i}(r) - \nu\sigma_{\theta\theta,i}(r) + \sigma_{zz,i}) \\ & + \alpha\Delta T \end{aligned} \quad [\text{A4b}]$$

where E , ν , and α are Young's modulus, Poisson's ratio, and CTE of the phase being considered, and ΔT is the temperature change. The constant axial strain ε_a is a third unknown.

Force equilibrium in the fiber axial direction yields

$$\begin{aligned} \int_0^{R_f} \sigma_{zz,f} \cdot r \cdot dr + \int_{R_f}^{R_l} \sigma_{zz,l} \cdot r \cdot dr \\ + \int_{R_l}^{R_m} \sigma_{zz,m} \cdot r \cdot dr = 0. \end{aligned} \quad [\text{A5}]$$

Substituting for each of the three layers from Eq. [A4b] and simplifying using Eqs. [A2a] and [A2b], we have

$$A_1 \cdot \varepsilon_a + B_1 \cdot a_1 + C_1 \cdot b_1 = D_1 \quad [\text{A6}]$$

where A_1 , B_1 , C_1 , and D_1 are constants, functions of the materials properties.

Compatibility of radial displacement (u_i) at the fiber-layer and layer-matrix interfaces gives

$$u_f = u_l \quad \text{at } r = R_f \quad [\text{A7a}]$$

$$u_l = u_m \quad \text{at } r = R_l. \quad [\text{A7b}]$$

Since $u = r \cdot \varepsilon_{\theta\theta}$, Eqs. [A2a], [A2b], [A4a], [A4b], [A7a], and [A7b] yield

$$A_2 \cdot \varepsilon_a + B_2 \cdot a_l + C_2 \cdot b_l = D_2 \quad [\text{A8a}]$$

$$A_3 \cdot \varepsilon_a + B_3 \cdot a_l + C_3 \cdot b_l = D_3 \quad [\text{A8b}]$$

where A_2 , A_3 , B_2 , B_3 , C_2 , C_3 , D_2 , and D_3 are constants, functions of the materials properties.

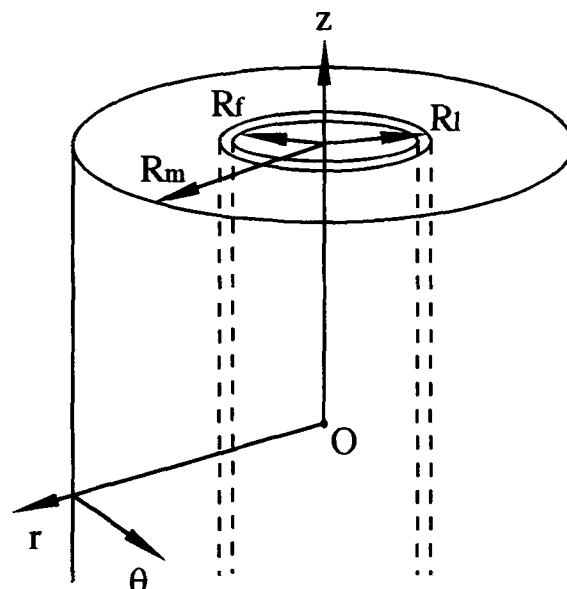


Fig. A1—Three-cylinder model: fiber (f), interphase layer (l), and matrix (m).

Equations [A6], [A8a], and [A8b] form a linear system of three equations with unknowns ε_a , a_l and b_l . Solving for these unknowns, the stresses in any of the three layers after any thermal path can be obtained by using equations [A2a] and [A2b] and the continuity relations [A3b] and [A3c].

APPENDIX B

Temperature dependence of materials thermomechanical properties

A. SCS-6 SiC Fiber

Between 20 °C and 940 °C, the Young's modulus and Poisson's ratio are constant and equal to $E = 400$ GPa and $\nu = 0.25$, respectively, and the CTE varies between $\alpha = 3.53 \cdot 10^{-6} \text{ K}^{-1}$ at 25 °C and $\alpha = 4.59 \cdot 10^{-6} \text{ K}^{-1}$ at 900 °C.^[16]

B. Ti-6Al-4V Matrix

The Poisson's ratio $\nu = 0.325$ ^[43] is assumed temperature independent. The yield strength at temperatures below 700 °C and the Young's modulus at temperatures below 500 °C are given in Reference 10. The values for the Young's modulus at temperatures above 500 °C are calculated using the temperature dependence of the shear modulus for unalloyed titanium.^[44] The coefficient of thermal expansion as a function of temperature is given by Touloukian *et al.*^[21]

C. TiC Interphase

As reported in References 45 through 49, the main reaction product between SCS-6 fibers and Ti-6Al-4V is TiC, since the fiber outer surface consists of a carbon-rich phase; other reaction products include various titanium silicides. We assume here that the interphase

consists of TiC, with Poisson's ratio $\nu = 0.188$ and CTE $\alpha = 7.5 \cdot 10^{-6} \text{ K}^{-1}$,^[22] assumed to be temperature independent. The Young's modulus is assumed to vary linearly with temperature between the two values given in the same reference: $E = 466 \text{ GPa}$ at $25 \text{ }^\circ\text{C}$ and $E = 344 \text{ GPa}$ at $1000 \text{ }^\circ\text{C}$. The thickness of the interphase (R_f) is taken as $2.5 \text{ } \mu\text{m}$; varying this value between $1 \text{ } \mu\text{m}$ and $5 \text{ } \mu\text{m}$ does not significantly affect the computed matrix stresses.

ACKNOWLEDGMENTS

This research was sponsored by the Délégation Générale pour l'Armement (France). We gratefully acknowledge Professors R.G. Ballinger and S. Brown from MIT for use of experimental facilities and Professors R.M.N. Pelloux and S. Suresh from MIT for helpful discussions.

REFERENCES

- D.C. Dunand and B. Derby: in *Fundamentals of Metal Matrix Composites*, S. Suresh, A. Mortensen, and A. Needleman, eds., Butterworth-Heinemann, Boston, MA, 1993, pp. 191-214.
- A.M. Ritter, F. Clark, and P. Dupree: in *Light Weight Alloys for Aerospace Applications II*, E.W. Lee and N.J. Kim, eds., TMS, Warrendale, PA, 1991, pp. 403-12.
- S.M. Russ: *Metall. Trans. A*, 1990, vol. 21A, pp. 1595-1602.
- W.C. Revelos and P.R. Smith: *Metall. Trans. A*, 1992, vol. 23A, pp. 587-95.
- S. Mall and P.G. Ermer: *J. Comp. Mater.*, 1991, vol. 25, pp. 1669-86.
- R.A. MacKay: *Scripta Metall. Mater.*, 1990, vol. 24, pp. 167-72.
- T.P. Gabb, J. Gayda, and R.A. MacKay: *J. Comp. Mater.*, 1990, vol. 24, pp. 667-86.
- Y.H. Park and H.L. Marcus: in *Mechanical Behavior of Metal-Matrix Composites*, J.E. Hack and M.F. Amateau, eds., TMS-AIME, Dallas, TX, 1982, pp. 65-75.
- Y. LePetitcorps, R. Pailler, and R. Naslain: in *Advanced Materials Research and Developments for Transport-Composites—1985*, P. Lamicq, W.J.G. Bunk, and J.G. Wurm, eds., Les Editions de Physique, Strasbourg, France, 1985, pp. 147-52.
- Smithells Metals Reference Book*, 7th ed., E.A. Brandes and G.B. Brook, eds., Butterworth-Heinemann, Oxford, United Kingdom, 1992, pp. 22.86-22.88.
- C.R. Brooks: *Heat Treatment, Structure and Properties of Nonferrous Alloys*, ASM, Metals Park, OH, 1982, pp. 331-39.
- B. Champin, L. Graff, M. Armand, G. Béranger, and C. Coddet: *J. Less-Common Met.*, 1980, vol. 69, pp. 163-68.
- P. Sarrazin and C. Coddet: *Corrosion Sci.*, 1974, vol. 14, pp. 83-89.
- C. Coddet, P. Sarrazin, and J. Besson: *J. Less-Common Met.*, 1977, vol. 51, pp. 1-12.
- R.A. Naik: NASA-CR-187599, 1991.
- S.M. Arnold, V.K. Arya, and M.E. Melis: NASA-TM-103204, 1990.
- J.T. Boyle and J. Spence: in *Stress Analysis for Creep*, Butterworth and Co., Oxford, United Kingdom, 1983, pp. 39-43.
- Y.M. Tarnopol'skii and T. Kincis: *Static Test Methods for Composites*, Van Nostrand, New York, NY, 1985, pp. 220-81.
- Annual Book of ASTM Standards*, ASTM, Philadelphia, PA, 1990, pp. 721-27.
- S.M.L. Sastry, P.S. Pao, and K.K. Sankaran: in *Titanium '80 Science and Technology*, H. Kimura and O. Izumi, eds., TMS, Warrendale, PA, 1980, pp. 873-86.
- Y.S. Touloukian, R.K. Kirby, R.E. Taylor, and P.D. Desai: *Thermophysical Properties of Matter, Vol. 12: Thermal Expansion of Metallic Elements and Alloys*, Plenum, New York, NY, 1975, pp. 346-53.
- CRC Materials Science and Engineering Handbook*, J. Shackelford and W. Alexander, eds., CRC Press, Boca Raton, FL, 1992, pp. 357-73.
- R.A. Schapery: *J. Comp. Mater.*, 1968, vol. 2, pp. 380-404.
- R.T. Bhatt and M.D. Kraitman: NASA-TM-86981, 1985.
- R.P. Nimmer, R.J. Bankert, E.S. Russell, and G.A. Smith: *J. Comp. Tech. Res.*, 1989, vol. 13, pp. 3-13.
- J.F. Durodola and B. Derby: *Acta Metall. Mater.*, 1994, vol. 42, pp. 1525-34.
- B.N. Cox, M.R. James, D.B. Marshall, and J.R.C. Addison: *Metall. Trans. A*, 1990, vol. 21A, pp. 2701-07.
- J. Lemaitre and J.L. Chaboche: *Mechanics of Solid Materials*, Cambridge, United Kingdom, 1990, p. 475.
- L. Wagner and G. Lütjering: *Z. Metallkd.*, 1987, vol. 78, pp. 369-75.
- R.P. Wei and D.L. Ritter: *J. Mater.*, 1972, vol. 7, pp. 240-50.
- H.W. Rosenberg, J.C. Chestnutt, and H. Margolin: in *Application of Fracture Mechanics for Selection of Metallic Structural Materials*, J.E. Campbell, W.W. Gerberich, and J.H. Underwood, eds., ASM, Metals Park, OH, 1982, pp. 213-52.
- J.W. Swanson and H.L. Marcus: *Metall. Trans. A*, 1978, vol. 9A, pp. 291-93.
- C.E. Shamblen and T.K. Redden: in *The Science, Technology and Application of Titanium*, R.I. Jaffee and N.E. Promisel, eds., Pergamon, Oxford, United Kingdom, 1968, pp. 199-208.
- M. Dechamps and P. Lehr: *J. Less Common Met.*, 1977, vol. 56, pp. 193-207.
- Alloy Phase Diagrams*, ASM, Metals Park OH, 1992, pp. 2-324.
- S. Suresh: *Fatigue of Materials*, Cambridge University Press, Cambridge, United Kingdom, 1991, pp. 1-511.
- B.J. Smith and A.R. Marder: *J. Eng. Mater. Technol.*, 1992, vol. 114, pp. 265-69.
- S. Suresh, G.F. Zamiski, and R.O. Ritchie: *Metall. Trans. A*, 1981, vol. 12A, pp. 1435-43.
- W. Oldfield and F.M. Oldfield: *Metall. Trans. A*, 1993, vol. 24A, pp. 2313-19.
- G.E. Dieter: *Mechanical Metallurgy*, McGraw-Hill, New York, NY, 1986, pp. 362-64.
- S.P. Timoshenko and J.N. Goodier: *Theory of Elasticity*, McGraw-Hill, New York, NY, 1976, pp. 65-69.
- J.A. Nairn: *Polymer Composites*, 1985, vol. 6, pp. 123-30.
- R.A. Wood: *Titanium Alloys Handbook*, MCIC, Columbus, OH, 1972.
- H.J. Frost and M.F. Ashby: *Deformation-Mechanism Maps*, Pergamon Press, Oxford, United Kingdom, 1982, pp. 44-45.
- C. Jones, C.J. Kiely, and S.S. Wang: *J. Mater. Res.*, 1989, vol. 4, pp. 327-35.
- T. Onzawa, A. Suzumura, and J.H. Kim: in *Composites—Design, Manufacture and Application*, S.W. Tsai and G.S. Springer, eds., SAMPE, Covina, CA, 1991, pp. 19.J1-19.J10.
- H.J. Dudek, R. Leucht, R. Borath, and G. Ziegler: *Microchim. Acta*, 1990, vol. II, pp. 137-48.
- C.G. Rhodes and R.A. Spurling: in *Recent Advances in Composites in the United States and Japan*, ASTM STP 864, J.R. Vinson and M. Taya, eds., ASTM, Philadelphia, PA, 1985, pp. 585-99.
- M. Lancin, J.S. Bour, and J. Thibault-Desseaux: in *High Temperature/High Performance Composites*, F.D. Lemkey, S.G. Fishman, A.G. Evans, and J.R. Strife, eds., MRS, Pittsburgh, PA, 1988, vol. 120, pp. 351-56.